Optimizing the network topology of block copolymer liquid crystal elastomers for enhanced extensibility and toughness

Christian Nowak and Fernando A. Escobedo
School of Chemical and Biomolecular Engineering, Cornell University, Ithaca, New York 14853, USA
(Received 28 January 2017; revised manuscript received 4 May 2017; published 2 August 2017)

Molecular simulations are used to study the effect of synthesis conditions on the tensile response of liquid-crystalline elastomers formed by block copolymer chains. Remarkably, it is found that despite the significant presence of trapped entanglements, these networks can exhibit the sawtooth tensile response previously predicted for ideal unentangled networks. It is also found that the monomer concentration during crosslinking can be tuned to limit the extent of entanglements and inhomogeneities while also maximizing network extensibility. It is predicted that networks synthesized at a "critical" concentration will have the greatest toughness.

DOI: 10.1103/PhysRevMaterials.1.035601

I. INTRODUCTION

Elastomers, crosslinked networks of polymer chains, often possess high extensibility but low toughness γ, the energy absorbed upon deformation before breakage. While increasing crosslinking density increases the Young's modulus, it also decreases extensibility and may not necessarily enhance γ [1,2]. It is thus desirable but challenging to develop elastomers with high γ that are also highly extensible; such materials would be appealing for applications requiring supertoughness such as specialty fibers, shock absorbers, artificial muscles, etc. This combination of properties has been predicted to be exhibited by model liquid crystalline elastomers (LCEs) with unentangled, tetra-functional crosslinking (T-LCE) and ABA block copolymers connecting the crosslinks [3,4]. These T-LCEs achieve that feat by producing a sawtooth shaped stress-strain response to uniaxial deformation, wherein each "tooth" is associated with microscopic rearrangements that increase the number of AB layers along the strain axis. A key question to be addressed by this study is whether realistic crosslinking schemes that generate complex and defective connectivities [5] can also lead to elastomers with high toughness and extensibility.

LCE are elastomers where the constituent chains are semiflexible, i.e., have a large persistence length $l_p \sim 100$ Å, that form orientationally aligned liquid crystal phases induced by various stimuli [6–10]. In LCEs, network deformation is coupled to chain orientation [6], a feature that can be exploited in artificial muscles [11,12] and high-strain actuators [13,14]. T-LCE are LCE where, under full 3D extension, tetra-functional crosslinks would sit on the lattice points of a diamond lattice with the homopolymers acting as the carbon bonds in diamond. Due to main-chain backbone semiflexibility, the chains and crosslinks self-assemble into separate layers (Fig. 1) [4,15,16]. Upon uniaxial deformation, stress builds in these networks until chain backbone hairpins unfold and a new crosslink layer forms. For semiflexible polymers, the mechanism of chain unfolding entails "shifting" the mass of one hairpin leg to the other leg until the first leg is short enough that the bending energy overcomes entropy and full unfolding occurs [17]. Upon hairpin unfolding, the network "yields," to reduce chain overstretching, and a new layer is formed. For T-LCE, hairpin unfolding is further hindered by the crosslinking of chain ends, and the entropic segregation of the crosslinks that is broken during unfolding. For T-LCE with ABA block copolymer chains, the addition of an interfacial energy penalty enhances the segregation, and favors the formation of smectic (orientationally and translationally ordered) domains of A and B blocks [3,4]. While forming a new domain, the surface area and, consequently, the interfacial energy, increases, requiring larger stresses for domain formation as compared to homopolymer T-LCE. Further deformation leads to a succession of large stress peaks giving the characteristic sawtooth stress-strain pattern [3,4]. This deformation mechanism is reminiscent of naturally occurring tough materials such as titin and spider silk, both of which undergo nonaffine domain deformations to relieve stress [18–23]. The concept of yielding to allow for greater energy absorption is the cornerstone of the "crumple zone," a concept used in cars and protective equipment [24,25].

T-LCEs embody a particular type of model network topology wherein tetra-functional sites are interconnected as in a single diamond lattice, but the sawtooth tensile response is not expected to be a unique characteristic of such a topology. In fact, other LCE topologies with regular lattice connectivity such as double gyroid and double diamond have also been shown to produce sawtooth tensile responses [16]. But such model LCEs (including T-LCE) represent the limiting case of perfect, unentangled networks; in contrast, both natural and synthetic LCEs exhibit topological inhomogeneities and entanglements that affect the tensile response [26–30]. Indeed, entanglements tend to impede crosslink mobility which is vital to the formation of multiple domains, and reduce network extensibility α_m = maximum strain before stress divergence (when further domain formation does not restore the stress to ~0), limiting the amount of energy that can be absorbed during deformation [31].

In reaction schemes of flexible chain networks where the chains end-link with crosslinking molecules, different types of spatial/topological inhomogeneities develop, e.g., "self-biting" occurs when both ends of a chain react with the same crosslink. LCEs can exhibit additional microstructural defects like polydomains, which arise from a localized alignment of chains along distinct directors in different regions of the network, and degrade the mechanical properties [32–34]. In a preliminary simulation study of ABA block copolymer chains end-linked with tetra-functional monomers, the sawtooth

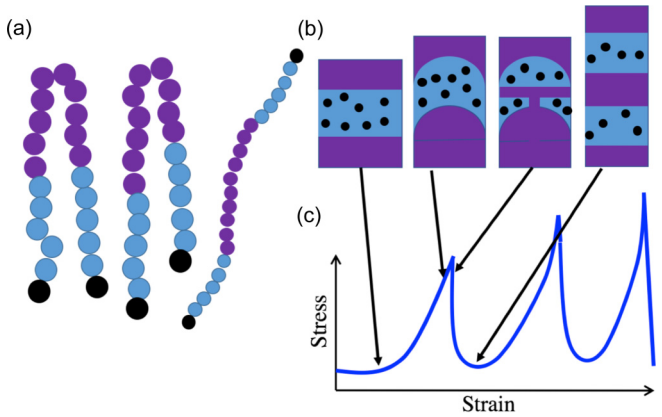

FIG. 1. (a) Depiction of unfolding mechanism for semiflexible chains (colored as block copolymer for clarity). Unequal pull on the ends of the hairpin aids to the release of bending energy by unfolding. (b) Cartoon of the stress built-up and release mechanism in T-LCE with block copolymer chains, describing states around a representative tooth in the stress-strain curve (c). *From left to right:* The applied strain first removes any "slack" in the system, and begins to deform the llamella, increasing the interfacial energy and the stress. After a greater amount of strain, the hairpins begin to unfold, breaking the parent layer into two daughter layers, and relaxing the stress.

tensile behavior found in T-LCEs was largely suppressed [16], likely due to the presence of defects and entanglements. With the goal of approaching ideal tetra-functional connectivity elastomers, a recently developed protocol uses two tetra-functional molecules that have either one of two reactive end groups (amine terminated, or N-hydroxysuccinimide terminated, depicted in Fig. 2) [35,36]. Herein we refer to these tetra-functional molecules as monomers (type 1 or type 2, as depicted in Fig. 1) and their arm lengths as l_a. Type 1/2 monomers can only react with type 2/1 monomers, preventing both self-biting and the formation of "loops" having an odd number of monomers, which improves mechanical properties [37]. A loop is defined as a connected path that starts from one given monomer and traces a path along connected monomers that ends at the starting monomer. n loops are defined as loops that contain "n" monomers along the path. We will refer to this reaction scheme as the "AB tetra-monomer" (ABTAM) method.

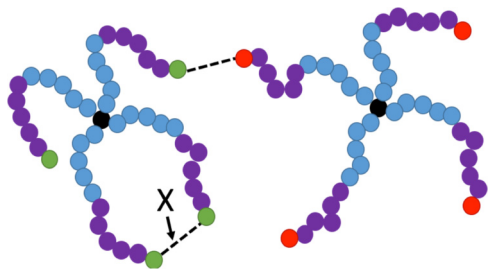

FIG. 2. Schematic of ABTAM reaction. Each monomer consists of a tetra-functional crosslink (black), connected by the A block (blue) of an AB block copolymer (B block is purple). There are two monomer types differentiated by the end-group on the chains (type 1 is red, type 2 is green). Only end-beads of different colors can bond.

Using molecular dynamics, this study aims to determine if realistic LCE networks, denoted as R-LCE, formed by the ABTAM protocol can exhibit the sawtooth tensile response observed in T-LCEs, and if so, which synthesis parameters create networks with optimized toughness and α_m.

II. MODELS AND METHODS

Below we describe the key aspects of our simulation model/methods. A more complete description can be found in the Supplemental Material (SM) [38]. The polymers are described as bead-spring chains [39,40] with beads bonded using a FENE potential [41]:

$$U_{\mathrm{FENE}} = -K\frac{R_0^2}{2}\ln\left[1-\left(\frac{r}{R_0}\right)^2\right] + 4\varepsilon\left[\left(\frac{\sigma_{\mathrm{LJ}}}{r}\right)^{12}-\left(\frac{\sigma_{\mathrm{LJ}}}{r}\right)^{6}+\frac{1}{4}\right], \quad (1)$$

where excluded volume interactions are described by the LJ-like potential term, that is cut off at $r = r_c = 2^{1/6}\sigma_{\mathrm{LJ}}$. The spring constant is $K = 30\varepsilon/\sigma_{\mathrm{LJ}}^2$ and the maximum bond extension is $R_0 = 1.5\sigma_{\mathrm{LJ}}$, which describe a stiff bond whose equilibrium length is approximately equal to the bead diameter ($\sim 0.97\sigma_{\mathrm{LJ}}$). For nonbonded interactions, there are four unique bead types: A(B) beads represent the A(B) block, and C(D) represents the reactive end beads on monomers of type 1(2). The tetra-functional bead is considered type A. A cut and shifted LJ potential is used with the form

$$U_{\mathrm{LJ}} = 4\varepsilon^{ij}\left[\left(\frac{\sigma_{\mathrm{LJ}}}{r}\right)^{12}-\left(\frac{\sigma_{\mathrm{LJ}}}{r}\right)^{6}-\left(\frac{\sigma_{\mathrm{LJ}}}{r_c}\right)^{12}+\left(\frac{\sigma_{\mathrm{LJ}}}{r_c}\right)^{6}\right] \quad (2)$$

for $r \leqslant r_c$ ($U_{\mathrm{LJ}} = 0$ otherwise), where $r_c^{ij} = 2.5\sigma_{\mathrm{LJ}}$ (attractive potential), when $i = j$, and $r_c^{ij} = 2^{1/6}\sigma_{\mathrm{LJ}}$ (repulsive potential), when $i \neq j$, and $\varepsilon^{ij} = 0.5\varepsilon$ for all interaction pairs ij. C and D beads interact through an additional Yukawa potential that is given in Eq. (S1) [38].

Chain stiffness is induced by a bending potential that is applied to all beads that are not bonded to a crosslink, which has the form

$$U_{\mathrm{angle}} = k_b T K_{\mathrm{bend}}(1+\cos\Psi), \quad (3)$$

where K_{bend} is a stiffness constant and ψ is the angle between two consecutive bond vectors; unless otherwise noted, $K_{\mathrm{bend}} = 4$.

Structurally, the monomers are composed of a tetra-functional crosslink connected to four AB block copolymer "arms" by the A block. The last bead in each arm is treated as C/D beads for type 1/2 monomers. Arm lengths of $l_a = 5$, 11, 15, 20, 40, 60, 80, and 100 beads were studied, with corresponding volume fractions of A of 0.4, 0.455, 0.467, 0.5, 0.5, 0.5, 0.5, and 0.5. χN values for chains formed when two arms bond together are 13.5, 35.0, 52.7, 71.0, 161.5, 251, 342.8, and 434.6 in order of increasing l_a [42]. To simulate the crosslinking reaction, when a C/D bead is within $1\sigma_{\mathrm{LJ}}$ distance of a D/C bead and both beads have yet to form a crosslinking bond, a bond is formed with a preset probability. Following experimental studies that optimized the mechanical properties

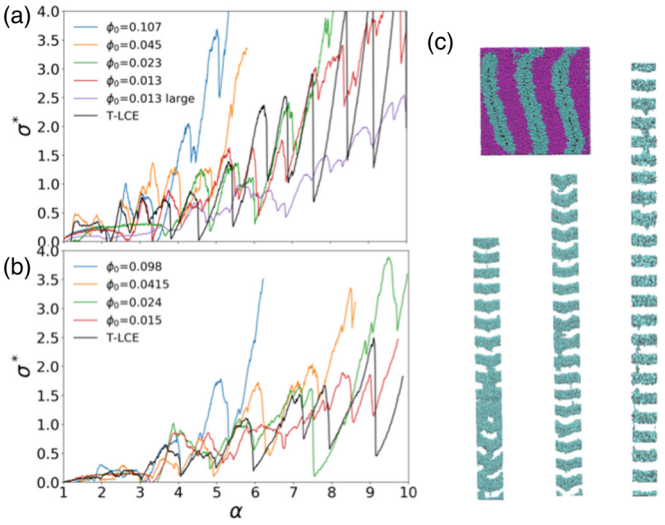

FIG. 3. Tensile plots of various ϕ_0 for $l_a = 11$(a) and $l_a = 20$ (b). (c) Snapshots from the deformation of a network synthesized from 4096 monomers at $\phi_0 = 0.0133$, for $\alpha = 1$, 4.7, 5.9, and 6.9 counterclockwise from the top left. Color scheme follows Fig. 1. For high α the B block is removed for clarity.

of synthesized networks [43,44], the two monomer types are at equal concentrations and the reaction rate is assumed to be kinetically limited (i.e., the probability of bond formation is low). Once initiated, the reaction proceeds until conversion reaches $\sim 96.5 - 97.5\%$. All results are for a good implicit solvent where both the A and B blocks of the monomers are well solvated, as would be the case if the solvent is a mix of two solvents, each selective for one block. Standard periodic boundary conditions are used throughout. Once synthesized, the networks are compressed from the synthesis concentration ϕ_0 to the prescribed melt density ϕ_{melt} and equilibrated [ϕ is defined as (number of beads)/σ_{LJ}^3]. For uniaxial deformation, we use an "iso-strain isobaric mixed ensemble" where the deformation axis has a prescribed strain while the orthogonal directions are controlled by a barostat [45].

III. RESULTS AND DISCUSSION

A. Effect of monomer concentration at crosslinking

Our simulations aim to quantify how network quality is affected by ϕ_0, the monomer concentration during crosslinking. ϕ_0 has a strong effect on the topological microstructure of the network: a small value can lead to inhomogeneous, poorly percolating networks, while a large value can lead to highly entangled systems. Synthesized networks of varying l_a and monomer concentration all microphase segregate into AB lamellae when compressed to ϕ_{melt}, regardless of ϕ_0; however, the lamellae plane normal generally does not point in the [100] direction due to a mismatch between the lamellar spacing and the simulation box size [46]. This leads to the deformation axis being initially misaligned with the director (the direction of chain alignment), which leads to "soft" low-stress initial deformations (see SM [38]) [47]. Figure 3 shows the tensile responses of several networks synthesized at different concentrations for $l_a = 11$ [Fig. 3(a)] and 20 [Fig. 3(b)].

After the soft regime, all curves approximately follow a characteristic pattern with ϕ_0 determining α_m. The toughness $\gamma_{\alpha=x}$ is defined as the area under the stress strain curve from $\alpha = 1$ to x (omitting negative stresses). We find that $\gamma_{\alpha=5} \sim 2.43$ for the R-LCE network with $l_a = 11$ and $\phi_0 = 0.045$, comparable to $\gamma_{\alpha=5} \sim 1.91$ for T-LCE. The microscopic mechanism underlying the sawtooth behavior is also fundamentally the same as that of the perfect network (summarized in the Introduction). The behavior changes when the stress starts to diverge, where, due to entanglements, enthalpic segregation of blocks and chain relaxation are hindered. At that point, chain disinterdispersion, hairpin unfolding, and phase segregation subside, and the tensile response becomes dominated by chain hyperextension and bond stretching. Indeed, near α_m, bond-stretch energy trends upward while interfacial energy is not a significant contributor to the stress as shown in Fig. S2 in the SM [38]. At very low ϕ_0 ($\phi < 0.01$ for $l_a = 11$) the connectivity of the network is significantly reduced compared to higher ϕ_0 cases ($\phi_0 > 0.1$ for $l_a = 11$) and may be affected by the finite size imposed by the boundary conditions. To clarify this effect, we simulated a network synthesized with 4096 monomers (8 times the 512 used for all other syntheses) at $\phi_0 = 0.0133$ and saw similar connectivity (Fig. S3 [38]). The tensile response of this network [Fig. 3(a) curve labeled "large" and Fig. 3(c)] shows peaks with smaller and less defined peaks. This is due to the longer relaxation time scales in larger networks, where the averaging of multiple transformations initiated at slightly different times leads to a smoothing out of the tensile response. This smoothing is expected to continue into the macroscopic regime, especially above a length scale where regions of different chain alignment form (known as polydomains) [32]. These domains will only be weakly coupled to each other at their boundaries, leading to further decoherence of the formation of new smectic domains in the sample, and to additional "averaging" of the tensile response.

Having established that the tensile response of R-LCEs approaches that of the T-LCE, we now examine how the microstructural details affect the tensile response. Figure 4(a) shows the number of 2, 4, and 6 loops normalized by the number of monomers. Figure 4(b) shows the equilibrium swelling volumes normalized to the swelling volume of a perfect network (swelling ratio $= SR$) and the chain ratio (CR) [48] (see SM for details [38]). CR compares the ensemble average of the minimum length a chain can have while still obeying topological entanglements (found by shrinking all chains till taut), to the minimum distance between the chain end points; thus, larger values of CR represent more entangled networks. SR provides a more macroscopic indicator of network quality, with smaller values pointing to more trapped entanglements.

Figures 4(a) and 4(b) show data for all arm lengths plotted against half the average monomer separation distance at ϕ_0, r_{sep} (based on nearest neighbors from Voronoi tessellation), normalized by the average end-to-end distance of individual chain arms r_{ee}. The ratio $r_{\text{sep}}/r_{\text{ee}}$ represents the separation distance relative to the distance where the monomers begin to "feel" each other and $r_{\text{sep}}/r_{\text{ee}} \approx 1$ can thus be seen as a probe of conditions consistent with the "overlap" concentration ϕ^*. At $r_{\text{sep}}/r_{\text{ee}} \approx 0.9$, there is an inflection at $CR \sim 1.05$, corresponding to $SR \approx 1$, at which point the number of 6 loops

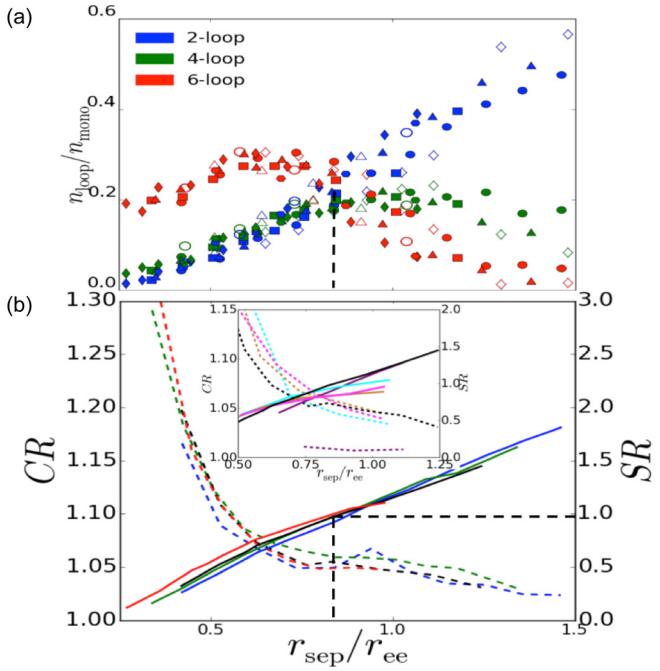

FIG. 4. The number of topological loops (a), *SR* (b), solid lines, and *CR* (b), dashed lines, for different l_a. In (a), $l_a = 5$, 11, 15, 20, 40, 60, 80, and 100 are represented by the open diamonds, filled circles, filled squares, filled triangles, filled diamonds, filled hexagons, open circles, and open triangles, respectively. In (b), $l_a = 11$, 15, 20, and 40 are colored blue, green, black, and red, respectively. In the inset, $l_a = 5$, 20 (for reference), 60, 80, and 100 are colored purple, black, cyan, brown, and pink, respectively. Black dashed lines outside of inset are used as guides to show that when $SR = 1$, there is an inflection point in *CR*.

start decreasing with decreasing ϕ_0, signaling a change in microstructure.

For $11 \leqslant l_a \leqslant 40$, two regimes of network topology as a function of ϕ_0 are postulated to explain these observations. The first topological regime corresponds to $r_{sep}/r_{ee} < 0.9$ [Figs. 4 and 5(a)], where increasing r_{sep}/r_{ee} (or decreasing ϕ_0) decreases the number of trapped entanglements n_e, because of the reduction in chain interpenetration during synthesis. Reducing n_e directly lowers both the *CR* and the effective crosslink density which translate into larger swelling. Also in this regime, the number of loops of any size decreases with decreasing r_{sep}/r_{ee} because higher concentrations increase the number of neighboring monomers, which reduces the probability of creating loops of any size. These trends continue until $r_{sep}/r_{ee} \approx 0.9$ [Fig. 5(b)], where the number of 6 loops is maximized, the $SR \approx 1$, and the *CR* curve has an inflection.

The second topological regime corresponds to $r_{sep}/r_{ee} > 0.9$ [Fig. 5(c)], where a fully connected network would result in chains that are overstretched and so the network collapses to allow chains to relax. In this regime, α_m is directly correlated to the number of 2 loops and inversely related to the number of 6 loops. If the probability of a loop becoming entangled is proportional to the loop "volume", 4 and 6 loops are more likely to become entangled compared to 2 loops, and are consequently more deleterious to a sawtooth, large α_m tensile response. Since larger loops are areas of stress localization during deformation

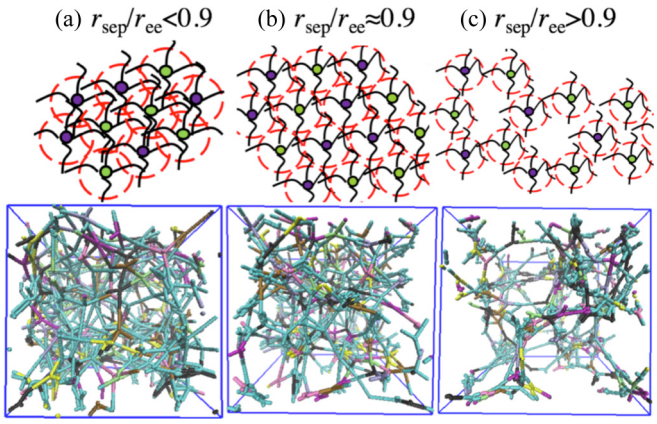

FIG. 5. Cartoons (top) of synthesis environment (red circles depict monomer coils of radius r_{ee}), and representative simulation snapshots after applying the chain ratio algorithm (bottom) for networks with $l_a = 11$ synthesized at $\phi_0 = 0.107$ (a), 0.045 (b), and 0.023 (c).

[35], both the increase in 2 loops and decrease in 4 and 6 loops lead to larger α_m. The inset of Fig. 4(b) shows that for $l_a = 5$ and $l_a = 60 - 100$ deviations from the two-regime trends discussed above become significant. Indeed, very short chains (of the order of the persistence length) entangle weakly over the range of ϕ_0 considered, while chains longer than some threshold [49] entangle more strongly for $r_{sep}/r_{ee} < 0.9$ than shorter chains. Henceforth, we only focus on systems with $5 < l_a < 60$.

To define an optimal ϕ_0, in Fig. 6 we plot α_m scaled by $\alpha_m^{ideal} = \alpha_m$ of a T-LCE with the same l_a, against r_{sep} scaled by r_{ee}. The plot is linear but plateaus for $r_{sep}/r_{ee} \geqslant 1$. These trends can be rationalized using a simple physical picture, by imagining the monomer coils as spheres of radius r_{ee}, and the overlap volume between spheres V_{cap}, as dictating n_e and consequently α_m. Since V_{cap} is largely linearly dependent on r_{sep} until plateauing at zero when $r_{sep} \geqslant r_g$, then the assumption that $n_e \propto V_{cap}$ provides predictions consistent with both the linear regime ($r_{sep}/r_{ee} < 1$) and the plateau regime (because for $r_{sep}/r_{ee} \geqslant 1$ there is zero overlap and n_e no longer

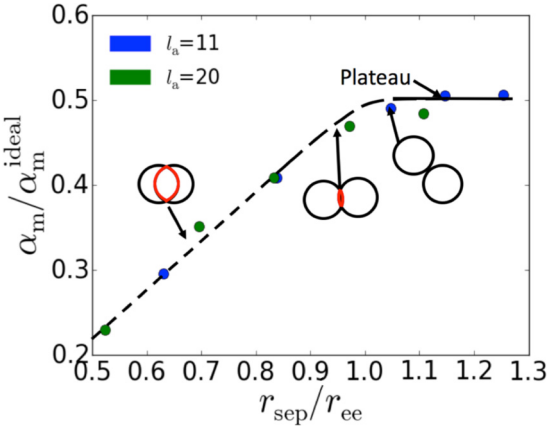

FIG. 6. Plot of the scaled extensibility against the r_{sep} normalized by r_{ee}. Circle cartoons represent the monomer spheres and their interacting regions (spherical caps in red).

decreases). As a result, R-LCEs synthesized at $r_{sep}/r_{ee} \sim 0.9$ are predicted to have the greatest toughness, by maximizing α_m, while still having an isotropic network connectivity. Such optimal conditions approximately correspond to $\phi_0 = 0.023$ and 0.012 for the networks with $l_a = 11$ and 20, respectively (see Fig. 2 for stress response and Fig. S2 in the SI [38] for representative snapshots).

The trends in Fig. 6 can also be explained by analyzing the behavior of the free energy "F" for an entangled network, according to the theory developed by Edwards and Vilgis [50]:

$$\frac{F}{k_B T} = \frac{N_c}{2}\left\{\frac{(1-a^2)\sum_{i=1}^{3}\alpha_i^2}{1-a^2\sum_{i=1}^{3}\alpha_i^2}\right\} + \frac{N_s}{2}\left\{\sum_{i=1}^{3}\left[\frac{\alpha_i^2(1+\eta)(1-a^2)}{\left(1+\eta\alpha_i^2\right)\left(1-a^2\sum_{i=1}^{3}\alpha_i^2\right)} + \ln\left(1+\eta\alpha_i^2\right)\right] + (1-N_c/N_s)\ln\left(1-a^2\sum_{i=1}^{3}\alpha_i^2\right)\right\}, \quad (4)$$

where a is the ratio of the length scale of a polymer random walk to the length scale of the primitive path, N_c is the number of crosslinks, N_s is the number of slip links, η is a measure of slippage, and α_i is the extension ratio of direction i. The criterion for maximum extensibility is when $dF/d(\alpha_x^2)$ diverges (taking x as the extensional direction). By taking the derivate of F with respect to α_x^2 and applying the constraint that α_x is large, we get

$$\frac{dF}{d\left(\alpha_x^2\right)} \propto \frac{N_c}{2}\left\{\frac{(1-a^2)}{1-a^2\alpha^2} - \frac{(1-a^2)a^2\alpha^2}{(1-a^2\alpha^2)^2} - \frac{a^2}{1-a^2\alpha^2}\right\} + \frac{N_s}{2}\left\{(1+\eta)(1-a^2)\left[\frac{a^2}{\eta(1-a^2\alpha^2)}\right] - \frac{a^2}{1-a^2\alpha^2}\right\}. \quad (5)$$

Equation (5) has two limits of interest: $a \sim 1$ (high entanglement) and $a \sim 0$ (no entanglement).

The limit $a \sim 0$ (no entanglement, large r_{sep}/r_{ee}) leads to

$$\frac{dF}{d\left(\alpha_x^2\right)} \sim \text{const.}, \quad (6)$$

which predicts the plateau observed in our results. For the $a \sim 1$, the expression simplifies to

$$\frac{dF}{d\left(\alpha_x^2\right)} \propto \frac{1}{\alpha^2 a^2}. \quad (7)$$

To maintain the same value of the derivative (i.e., the divergence slope for maximum extensibility) the product $a^2\alpha^2$ must remain the same, so $\alpha \propto 1/a$. Parameter a is inversely proportional to *CR*, and since Fig. 4(b) also showed that *CR* is roughly inversely proportional to r_{sep}/r_{ee} for $r_{sep}/r_{ee} < 0.9$, it follows that $\alpha_m \propto r_{sep}/r_{ee}$ (consistent with Fig. 6).

B. Effect of chain flexibility

Chain backbone stiffness is another key design parameter that affects the topological and tensile properties of the networks prepared using the ABTAM scheme. Since experimental studies have mostly focused on flexible polymers, we also simulated fully flexible chains. Our results for such systems indicate that the data for number of loops, *SR*, and *CR* all collapse onto similar curves as those reported before for semiflexible chains when using the r_{sep}/r_{ee} scaling. Unexpectedly, however, we also find that fully flexible chains cannot reproduce the distinctive sawtooth behavior seen for semiflexible chains (Fig. 7).

To decouple the effects of chain backbone and network topology on the tensile response, we prepared one network with "flexible topology" (taken from a synthesis where the chains were fully flexible) that was equilibrated and deformed in two different scenarios: one where the chains were still fully flexible (to be denoted the FF network), and one where the chains were now equilibrated as semiflexible (to be denoted the ESF network). Figure 8(a) shows the tensile response of the ESF network, exhibiting a sawtooth behavior which is qualitatively similar to the tensile response of a network with semiflexible chains from synthesis to deformation, shown by the line marked "SF" (the values of r_{sep}/r_g were matched for the two networks). This comparison indicates that the topology of fully flexible networks is not responsible for the lack of the sawtooth behavior.

To identify the key microstructural difference between the FF and ESF networks, we calculate the instantaneous root mean squared chain end-to-end distance of the full-length chains in the network. Using representative configurations from the deformations of the FF and ESF networks, the value of r_{ee} was calculated for each chain at two values of α, corresponding to before and after a "tooth" in the tensile response in ESF [as marked in Fig. 8(a)]. In Fig. 8(b) we plot the distribution of the absolute change in r_{ee} normalized by chain contour length $|\Delta r_{ee}|/l_c$, for both networks. The distribution for the FF network is largely unimodal while that for the ESF distribution has, besides a main unimodal chain population exhibiting small-to-moderate deformation, a subpopulation of chains undergoing very large unfolding, indicative of a less affine deformation. The degree of affine deformation is attributed to the way in which chains pack when they phase segregate. For the ESF/SF networks, the chains orientationally align (as expected of mesogenic chains) which leads to the formation of hairpins in the network. Mobility in

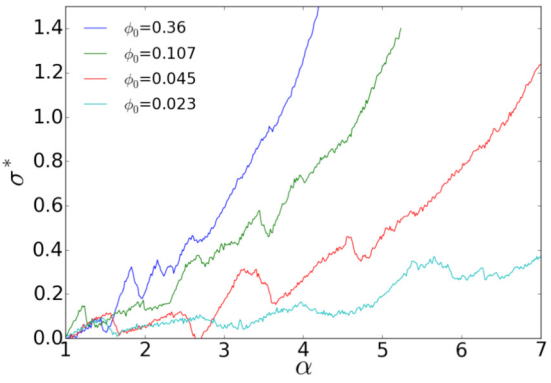

FIG. 7. The tensile response of synthesized flexible block copolymer networks with $l_a = 11$ for different ϕ_0.

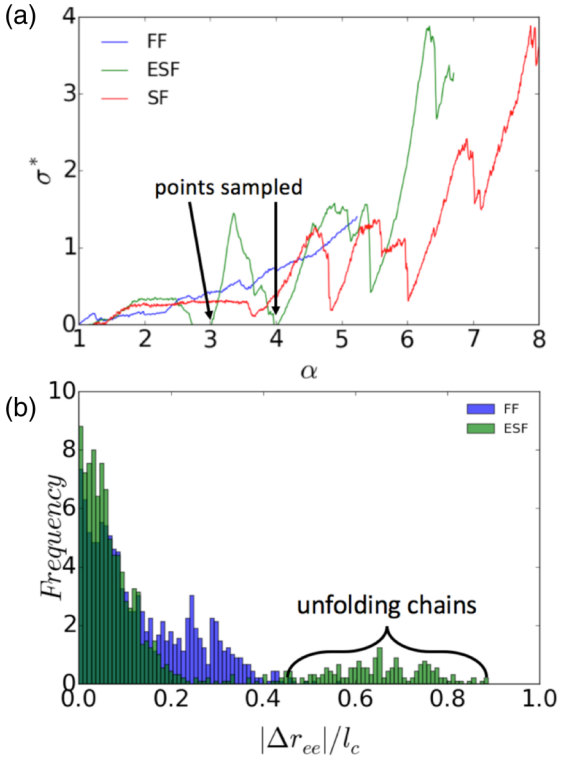

FIG. 8. (a) The tensile response of FF, ESF, and SF networks. "FF" and "ESF" ("equilibrated as SF") have identical network topologies. Note: the tensile response of the FF network is the same as that shown in Fig. 7 (for $\phi_0 = 0.107$). (b) Plot of the absolute change in r_{ee} normalized by l_c for all chains in the FF and ESF networks. The two values of α from which the configurations were sampled are marked by arrow in (a).

the melt along the deformation direction is required to unfold the chains, which is augmented by the nematic/smectic phases seen in T/R-LCE, where diffusion/mobility is greater along the director [51]. Orientational order also favors the complete unfolding of hairpins; in fact, the deformation predominantly occurs only where the new domain forms [associated with the population of chains with $|\Delta r_{ee}|/l_c > \sim 0.4$ in Fig. 8(b)]. In contrast, flexible chains do not orientationally order and any unfolding of hairpins will likely encounter obstructing chains and preclude localized deformations. Therefore, a fully flexible network undergoes more affine deformations (Fig. 7) as compared to semiflexible networks [Fig. 8(a)]. Additionally, because there are no "true" hairpins in the FF network, the mechanism of unfolding and new domain formation does not give "extra extension" to the network nor releases the stress abruptly, both key ingredients for a sawtooth tensile response.

IV. SUMMARY AND CONCLUSIONS

Unlike previous studies that detected sawtooth responses with idealistic network topologies, this work provides clear guidelines for engineering realistic, supertough elastomers, practicable via ABTAM-like approaches. Our R-LCEs achieve maximum extensibilities of $\alpha_m = 5$ and 8, and toughness values in the order of $\gamma_{\alpha=5} = 0.96$ and 0.52 GPa (assuming one unit of toughness is equal to 0.4 GPa [52]), for $l_a = 11$ and 20, respectively. Such values compare favorably to spider-dragline silk ($\alpha_{break} = 1.6$ [19] and toughness $\sim$0.15 GPa) and networks of PEO chains using ABTAM ($\alpha_{break} = 1.9$, and toughness $\sim$0.00023 GPa [43]).

The quality of the network topology produced by the ABTAM scheme depends crucially on the concentration during crosslinking ϕ_0. We have identified a microscopic metric that provides a tighter correlation with the network properties than ϕ_0: the average separation radius between monomers scaled by the arm end-to-end distance r_{sep}/r_{ee}. Our results suggest that networks synthesized at $r_{sep}/r_{ee} \approx 0.9$ provide the best combination of extensibility α_m and "quality" of the sawtooth tensile response. When r_{sep}/r_{ee} is increased, entanglements decrease and α_m increases, however, for $r_{sep}/r_{ee} > 0.9$, the reduction in entanglements abates and α_m plateaus.

We find that a two-regime trend for topological "quality" (Figs. 4 and 5) hold true for $5 < l_a < 60$ (which encompasses experimental ABTAM syntheses [43], e.g., degree of polymerization $\sim$50, equivalent to $l_a \sim 25$), for chains with persistence length of $\sim$4 (capable of accommodating liquid crystallinity) and for fully flexible chains. The local ordering and deformation mechanism of semiflexible chains leads to the nonaffine network deformations that are necessary for the sawtooth tensile response to occur.

ACKNOWLEDGMENTS

This work was supported by the National Science Foundation Award CMMI 1435852. This work used the Extreme Science and Engineering Discovery Environment (XSEDE), which is supported by National Science Foundation Grant No. ACI-1053575.

[1] A. Bandyopadhyay, P. K. Valavala, T. C. Clancy, K. E. Wise, and G. M. Odegard, Polymer **52**, 2445 (2011).
[2] T. L. Smith and J. E. Frederick, J. Appl. Phys. **36**, 2996 (1965).
[3] C. Nowak and F. A. Escobedo, Macromolecules **49**, 6711 (2016).
[4] B. M. Aguilera-Mercado, C. Cohen, and F. A. Escobedo, Macromolecules **47**, 840 (2014).
[5] K. Schwenke, M. Lang, and J.-U. Sommer, Macromolecules **44**, 9464 (2011).
[6] A. R. Tajbakhsh and E. M. Terentjev, Eur. Phys. J. E **6**, 181 (2001).
[7] M. Dijkstra and D. Frenkel, Phys. Rev. E **51**, 5891 (1995).
[8] G. Sigaud, D. Y. Yoon, and A. C. Griffin, Macromolecules **16**, 875 (1983).
[9] M. H. Li, P. Keller, B. Li, X. Wang, and M. Brunet, Adv. Mater. **15**, 569 (2003).
[10] D. Corbett and M. Warner, Sens. Actuators A **149**, 120 (2009).
[11] M. H. Li, P. Keller, J. Yang, and P. A. Albouy, Adv. Mater. **16**, 1922 (2004).
[12] H. Wermter and H. Finkelmann, e-Polymers **1**, 1 (2001).

[13] T. H. Ware, M. E. McConney, J. J. Wie, V. P. Tondiglia, and T. J. White, Science **347**, 982 (2015).
[14] H. Yang, A. Buguin, J. M. Taulemesse, K. Kaneko, S. Méry, A. Bergeret, and P. Keller, J. Am. Chem. Soc. **131**, 15000 (2009).
[15] D. M. Bhawe, C. Cohen, and F. A. Escobedo, Phys. Rev. Lett. **93**, 257804 (2004).
[16] B. M. Aguilera-Mercado, Ph.D. Thesis, Cornell University, 2012.
[17] D. R. M. Williams and M. Warner, J. Phys. **51**, 317 (1990).
[18] X. Wu, X. Y. Liu, N. Du, G. Xu, and B. Li, Appl. Phys. Lett. **95**, 093703 (2009).
[19] A. Nova, S. Keten, N. M. Pugno, A. Redaelli, and M. J. Buehler, Nano Lett. **10**, 2626 (2010).
[20] K. C. Ingham, S. A. Brew, S. Huff, and S. V. Litvinovich, J. Biol. Chem. **272**, 1718 (1997).
[21] E. Klotzsch, M. L. Smith, K. E. Kubow, S. Muntwyler, W. C. Little, F. Beyeler, G. Gourdon, B. Nelson, and V. Vogel, Proc. Natl. Acad. Sci. USA **106**, 18267 (2009).
[22] Z. H. Xu and X. Li, Adv. Funct. Mater. **21**, 3883 (2011).
[23] M. Rief, M. Gautel, F. Oesterhelt, J. M. Fernandez, and H. E. Gaub, Science **276**, 1109 (1997).
[24] A. Jung, L. A. A. Beex, S. Diebels, and S. P. A. Bordas, Mater. & Design **87**, 36 (2015).
[25] K. Hansen, N. Dau, F. Feist, C. Deck, R. Willinger, S. M. Madey, and M. Bottlang, Accident Anal. Prevent. **109**, 17 (2013)
[26] J. S. Biggins, M. Warner, and K. Bhattacharya, Phys. Rev. Lett. **103**, 037802 (2009).
[27] Z. Chen, C. Cohen, and F. A. Escobedo, Macromolecules **35**, 3296 (2002).
[28] D. M. Bhawe, C. Cohen, and F. A. Escobedo, Macromolecules **37**, 3924 (2004).
[29] K. Urayama, E. Kohmon, M. Kojima, and T. Takigawa, Macromolecules **42**, 4084 (2009).
[30] P. Dalhaimer, D. E. Discher, and T. C. Lubensky, Nat. Phys. **3**, 354 (2007).
[31] K. Urayama, T. Kawamura, and S. Kohjiya, Polymer **50**, 347 (2009).
[32] K. Urayama, Macromolecules **40**, 2277 (2007).
[33] J. Küpfer and H. Finkelmann, Makromol. Chem., Rapid Commun. **12**, 717 (1991).
[34] Z. Pei, Y. Yang, Q. Chen, E. M. Terentjev, Y. Wei, and Y. Ji, Nat. Mater. **13**, 36 (2014).
[35] M. Shibayama and T. Sakai, *Polymeric and Self Assembled Hydrogels: From Fundamental Understanding to Applications* (Royal Society of Chemistry, London, 2012), pp. 7–34.
[36] A. Sugimura, M. Asai, T. Matsunaga, Y. Akagi, T. Sakai, H. Noguchi, and M. Shibayama, Polym. J. **45**, 300 (2013).
[37] M. Asai, T. Katashima, U. I. Chung, T. Sakai, and M. Shibayama, Macromolecules **46**, 9772 (2013).
[38] See Supplemental Material at http://link.aps.org/supplemental/10.1103/PhysRevMaterials.1.035601 for additional information on simulation models and methods, calculations for network characterization, and expanded simulation results.
[39] G. S. Grest and K. Kremer, Phys. Rev. A **33**, 3628(R) (1986).
[40] S. C. Glotzer and W. Paul, Annu. Rev. Mater. Res. **32**, 401 (2002).
[41] K. Kremer and G. S. Grest, J. Chem. Phys. **92**, 5057 (1990).
[42] M.A. Horsch, Z. Zhang, C. R. Iacovella, and S. C. Glotzer, J. Chem. Phys. **121**, 11455 (2004).
[43] T. Sakai, T. Matsunaga, Y. Yamamoto, C. Ito, R. Yoshida, S. Suzuki, N. Sasaki, and U. I. Chung, Macromolecules **41**, 5379 (2008).
[44] K. Nishi, K. Fujii, Y. Katsumoto, T. Sakai, and M. Shibayama, Macromolecules **47**, 3274 (2014).
[45] M. Warner and E. M. Terentjev, *Liquid Crystal Elastomers* (Oxford University Press, Oxford, UK, 2007).
[46] F. J. Martínez-Veracoechea and F. A. Escobedo, J. Chem. Phys. **125**, 104907 (2006).
[47] P. D. Olmsted, J. Phys. II France **4**, 2215 (1994).
[48] S. K. Sukumaran, G. S. Grest, K. Kremer, and R. Everaers, J. Polym. Sci. Part B: Polym. Phys. **43**, 917 (2005).
[49] M. Pütz, K. Kremer, and G. S. Grest, Europhys. Lett. **49**, 735 (2000).
[50] S. F. Edwards and T. Vilgis, Polymer **27**, 483 (1986).
[51] A. A. Darinskii, A. Zarembo, N. K. Balabaev, I. M. Neelov, and F. Sundholm, Phys. Chem. Chem. Phys. **5**, 2410 (2003).
[52] E. Wang and F. A. Escobedo, Macromolecules **49**, 2375 (2016).